Electronic Supplementary Material (ESI) for RSC Advances.

Supporting Information

Preferential (100)-oriented $CH_3NH_3PbI_3$ perovskite films formation by flash drying and elucidation of formation mechanism

Se-Yun Kim,[a, b] Hyo-Jeong Jo,[b] Shi-Joon Sung,[b] Kang-Pil Kim,[b] Young-Woo Heo,[a] Dae-Hwan Kim*[b]

[a] School of Materials Science and Engineering, Kyungpook National University, Daegu, 702-701, South Korea

[b]Convergence Research Center for Solar Energy, Daegu-Gyeongbuk Institute of Science and Technology (DGIST), Daegu, 42988, South Korea

*Corresponding author: monolith@dgist.ac.kr

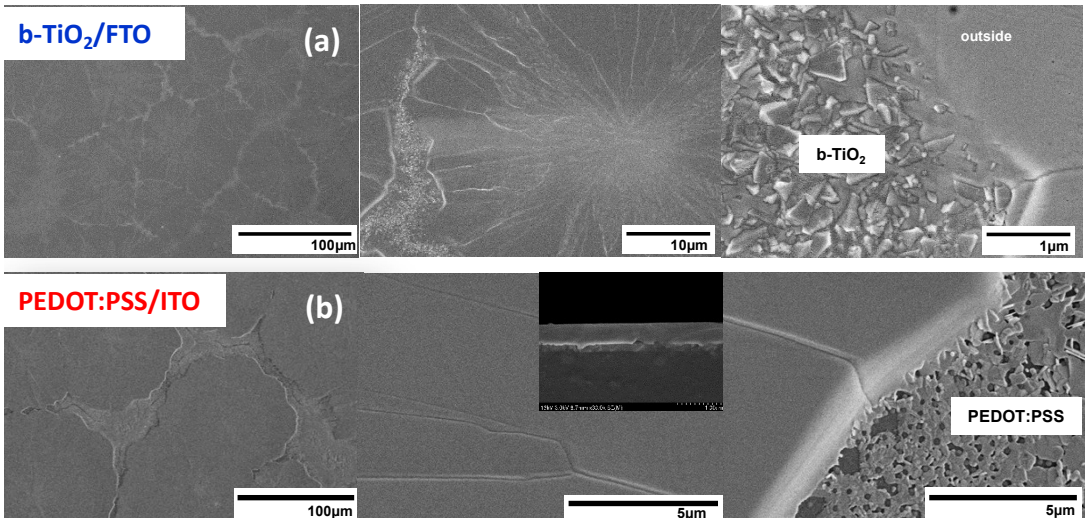

Figure S1. FESEM images of the perovskite films annealed at 150°C and formed on (a) b-TiO_2/FTO and (b) PEDOT:PSS/ITO substrates. 1 M solution of PbI_2 and MAI was spin-coated at 3000 rpm for 5 s on both substrates.

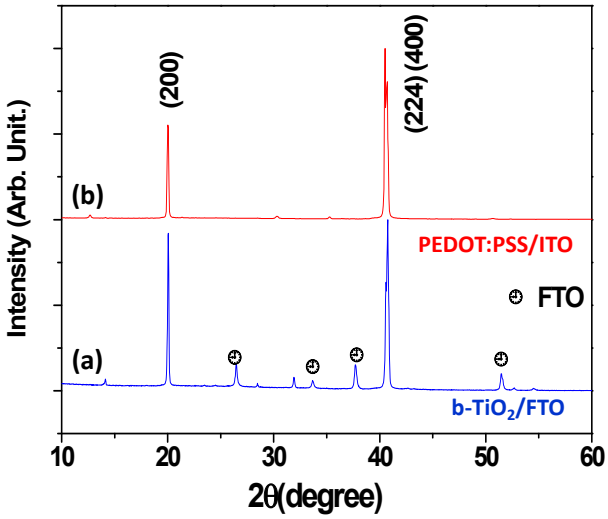

Figure S2. X-ray diffraction patterns of the perovskite films annealed at 100°C and formed on (a) b-TiO_2/FTO and (b) PEDOT:PSS/ITO substrates.

In this study, (100)-oriented perovskite films could be grown readily on PEDOT:PSS/ITO substrates by using a short spinning time, such as 5sec, and a relatively high annealing temperature. Figures S1 and S2 show FESEM images and the XRD patterns, respectively, of the perovskite films annealed at 100°C and grown on b-TiO_2/FTO and PEDOT:PSS/ITO substrates. The (100)-oriented perovskite layer was observed on both substrates. It was thus concluded that the growth orientation of the perovskite layer does not depend on the substrate used.

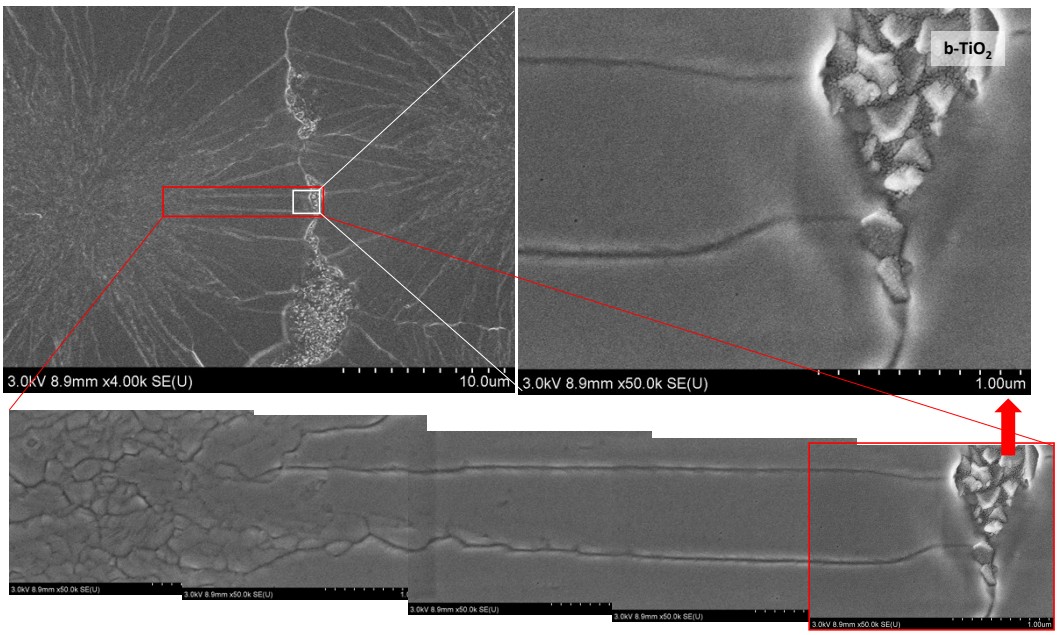

Figure S3 FESEM images of the perovskite film formed by 5s of spinning time and at 200°C of annealing temperature and 5sec of annealing time.

Fig S3 shows overlapping FESEM images of the perovskite film by 5s of spinning time and at 200°C of annealing temperature and 5sec of annealing time. From this high resolution FESEM images, the boundary in the images could be expected as grain boundary; the fine grains of b-TiO_2 layer was observed in the high resolution FESEM images.

HETERONUCLEATION THEORY

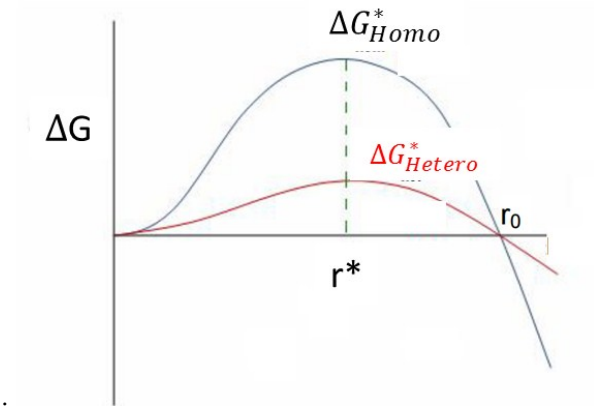

Figure S4. (a) The total free energy as a function of the nuclei radius is a sum of the volume free energy and the interfacial energy.

The value of ΔG_{homo}(free-energy change) at the instance when homonucleation from the liquid phase to the solid phase occurs can be determined from Eq.1 for the case where a spherical seed is formed; here, ΔG_V is the volume free energy, γ_{SL} is the interfacial energy of the seed, r is the nucleation radius, ΔG* is the free-energy barrier, and r* is the critical radius.

$$\Delta G_{homo} = \frac{4}{3}\pi r^3 \Delta G_V + 4\pi r^2 \gamma_{SL} \quad \text{(Eq. 1)}$$

$$\Delta G_{homo}^{*} = \frac{16\pi\gamma_{SL}^3}{3(\Delta G_V)^2} \quad \text{(Eq. 2)}$$

In the case when heteronucleation occurs, the free-energy change is given by Eqs. 3 and 4, where θ is the wetting angle and f(θ) is the shape factor ($0 < f(\theta) < 0.5$). (Ref: M. Ohring, Materials Science of Thin films (Deposition and Structure) 2nd edition (Book), Chapter 7)

$$\Delta G_{hetero}^{*} = \frac{16\pi\gamma_{SV}^3}{3(\Delta G_V)^2}\left(\frac{2-3\cos\theta+\cos^3\theta}{4}\right) \quad \text{(Eq.3)}$$

$$\Delta G_{hetero}^{*} = \Delta G_{homo}^{*} f(\theta) \quad \text{(Eq.4)}$$

According to this formula, ΔG_{hetero}^* decreases as the wetting angle decrease, with ΔG^* becoming zero when $\theta = 0°$. In other words, ΔG^* for heteronucleation is always smaller than that for homonucleation.

S5. RELATION BETWEEN DENSITY OF STABLE NUCLEI AND CONCENTRATION OF SOLUTE

$$N^* = n_s \exp(-\frac{\Delta G^*}{k_B T}) \quad \text{(Eq. 5)}$$

where N^* is the density of the stable nuclei, ΔG^* is the free-energy barrier, k_B is Boltzmann's constant, and T is the temperature. Further, n_s is the product of the impinging flux of atoms and their residence time. (Ref: R. J. Stokes, D. Fennell Evans, Fundamentals of Interfacial Engineering (Wiley-VCH), Chapter 10)

The change in the Gibbs free energy per unit volume of the solid phase, ΔG_V, is dependent on the concentration of the solute:

$$\Delta G_V = -\frac{kT}{\Omega}\ln(\frac{C}{C_0}) = -\frac{kT}{\Omega}\ln(1+\sigma) \quad \text{(Eq. 6)}$$

where C is the concentration of the solute, C_o is the equilibrium concentration or solubility, Ω is the atomic volume, and σ is the degree of supersaturation defined by $(C- C_o)/C_o$. Without supersaturation (i.e., when $\sigma = 0$), ΔG_V is zero, and nucleation does not occur. On the other hand, when C > Co, ΔG_V is negative and nucleation occurs spontaneously.

It should be noted that a higher degree of supersaturation (σ) leads to a decrease in the volume free energy (ΔG_V), which, in turn, leads to a decrease in the free-energy barrier (ΔG_{homo}^* or ΔG_{hetero}^*), as shown in Eqs. 2 and 4. Finally, the density of the stable nuclei increases when the degree of supersaturation increases, because N* depends exponentially on ΔG^*.

$$\Delta G_{homo}^* = \frac{16\pi\gamma_{SL}^3}{3(\Delta G_V)^2} \quad \text{(Eq. 2)}$$

$$\Delta G_{hetero}^* = \Delta G_{homo}^* f(\theta) \quad \text{(Eq.4)}$$

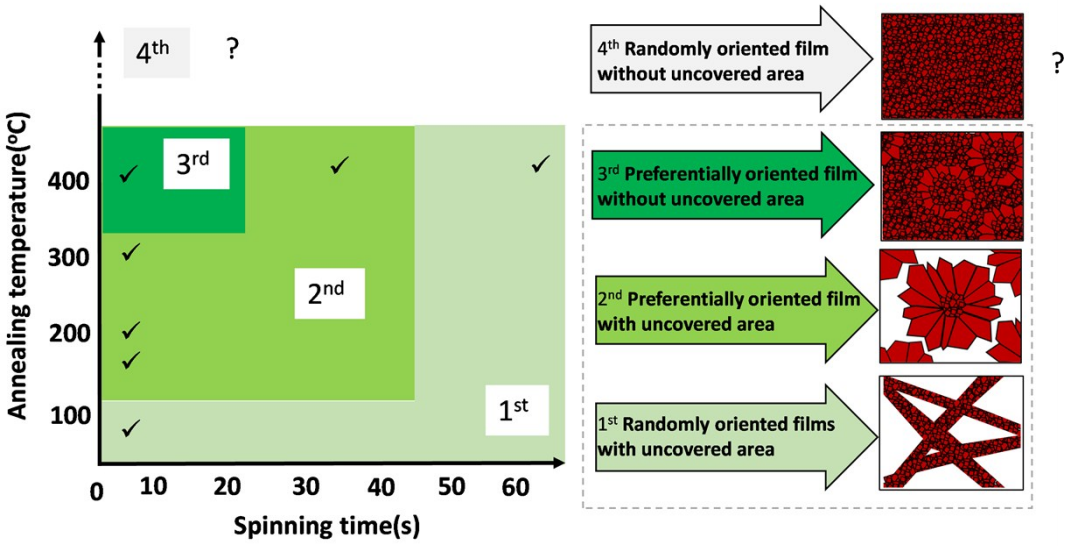

Fig. S6. Schematics of the four types of perovskite film microstructures formed for different annealing temperatures and spinning times.

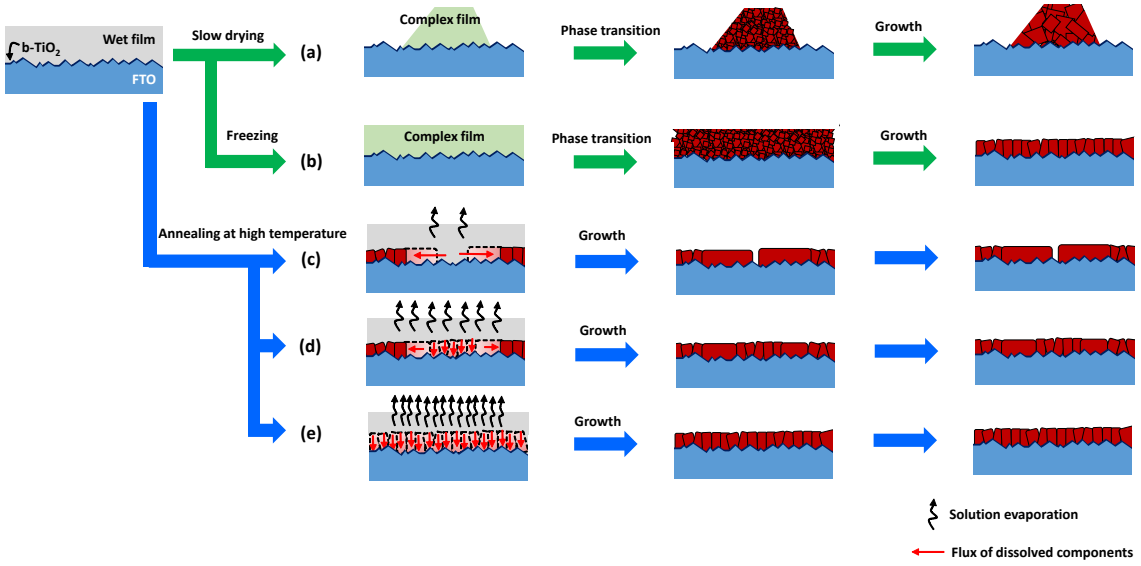

Fig. S7. Illustrations of the formation mechanisms of the (a) randomly oriented films with uncovered areas, (b) randomly oriented films without uncovered areas by freezing, (c) preferentially (100)-oriented films with uncovered areas, (d) preferentially (100)-oriented films without uncovered areas, and (e) randomly oriented films without uncovered areas. The illustration of the semi-dried complex films on the substrate was drawn at the left side and final films after annealing was drawn at the right side of the Fig. S6 (a) and (b). The illustration of the initial stage of the annealed wet-film was drawn at the left side, and the final stage of the annealed film was drawn at the right side of Fig. S6 (c), (d) and (e).

There is a competition between the lateral growth of the (100)-oriented grains and additional nucleation owing to supersaturation at 400°C. This is what causes the growth of the randomly oriented films without uncovered areas at annealing temperatures higher than 400°C.

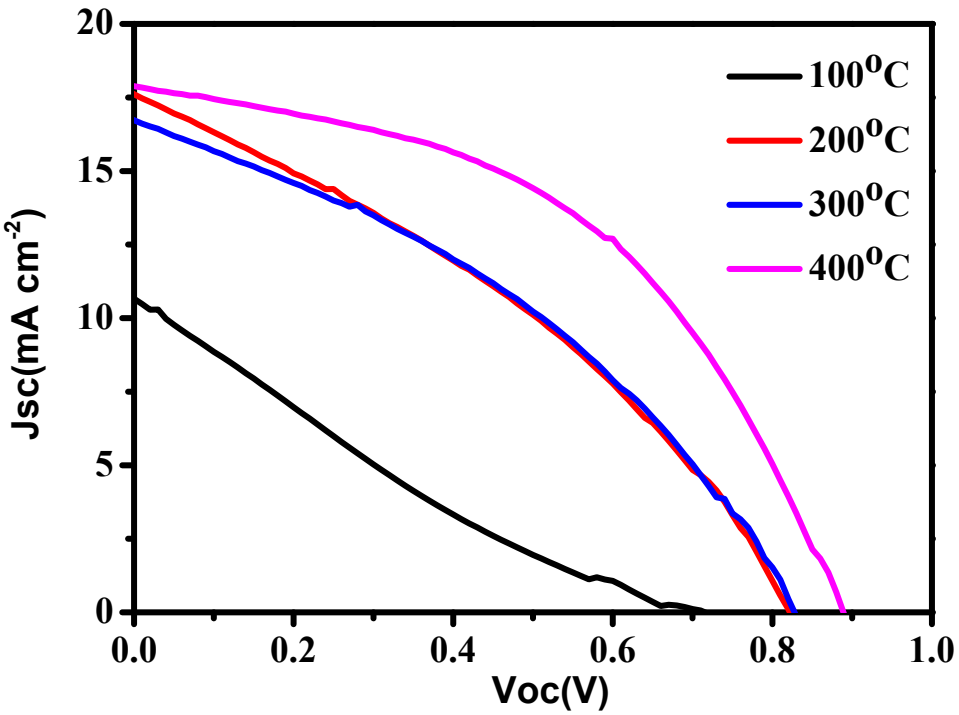

Fig. S8. Characteristic photocurrent-voltage plots of the solar cells based on the perovskite films formed at the different annealing temperatures (100, 200, 300, and 400°C). The average values for the negative and positive scans are shown.

That the efficiency of the device based on the perovskite film annealed at 400°C was the highest can be explained on the basis of the increased coverage of the film.

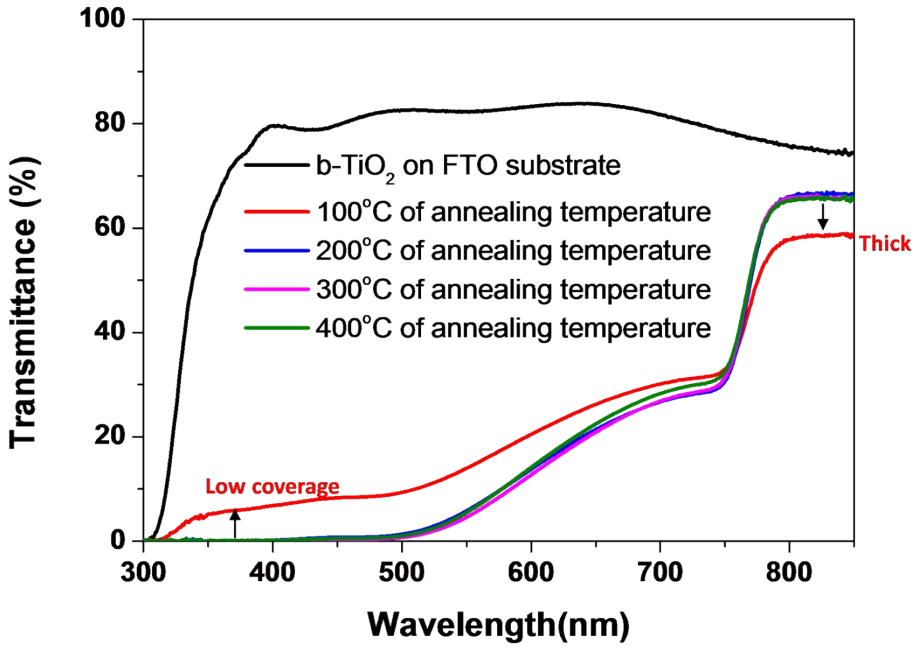

Fig S9. Transmittance spectra of the perovskite films formed on a b-TiO2 layer at annealing temperatures of 100, 200, 300, and 400°C.

Figure shows the transmittance spectra of the perovskite films formed on a b-TiO_2 layer at annealing temperature of 100, 200, 300 and 400°C. The similar spectra from 400nm to 750nm have been reported in perovskite absorber layer (Adv. Sci. 2016, 3, 1500324). The effect of low coverage with thick layer (the first type perovskite film at100°C of annealing temperature) on transmittance property was observed (*Molecules* 2016, *21*(4), 475). However, it was difficult to describe the effect of microstructure on UV-vis properties of second (200 and 300°C) and third (400°C) type of perovskite films, because the transmittance spectra of the samples (200, 300 and 400°C) were too similar.